POLITECNICO DI TORINO
Repository ISTITUZIONALE

Reliability of the geometric calibration of an hyperspectral frame camera

Original
Reliability of the geometric calibration of an hyperspectral frame camera / Musci, M.A., Aicardi, I., Dabove, P., Lingua, A.M.. - STAMPA. - 42:(2019), pp. 1701-1707. (4th ISPRS Geospatial Week 2019 nld 2019) [10.5194/isprs-archives-XLII-2-W13-1701-2019].

Availability:
This version is available at: 11583/2737436 since: 2019-06-26T15:45:00Z

Publisher:
International Society for Photogrammetry and Remote Sensing

Published
DOI:10.5194/isprs-archives-XLII-2-W13-1701-2019

Terms of use:

This article is made available under terms and conditions as specified in the corresponding bibliographic description in the repository

Publisher copyright

(Article begins on next page)

26 November 2026

RELIABILITY OF THE GEOMETRIC CALIBRATION OF AN HYPERSPECTRAL FRAME CAMERA

Maria Angela Musci [1, 2, *], Irene Aicardi[1, 2], Paolo Dabove[1, 2], Andrea Maria Lingua[1, 2]

[1] DIATI, Politecnico di Torino, Torino, Italy, 10124 Corso Duca degli Abruzzi,24 Torino – {mariaangela.musci, irene.aicardi, paolo.dabove, andrea.lingua}@polito.it
[2] PIC4SeR, Politecnico di Torino Interdepartmental Centre for Service Robotics, Torino, Italy

Commission I, WG IX/9

KEY WORDS: Camera Calibration, Hyperspectral Frame Camera, Fabry–Perot Interferometer, Photogrammetry.

ABSTRACT:

One of the main tools for high resolution remote sensing and photogrammetry is the lightweight hyperspectral frame camera, that is used in several application areas such as precision agriculture, forestry, and environmental monitoring. Among these types of sensors, the Rikola (which is based on a Fabry–Perot interferometer (FPI) and produced by Senop) is one of the latest innovations. Due to its internal geometry, there are several issues to be addressed for the appropriate definition and estimation of the inner orientation parameters (IOPs). The main problems concern the possibility to change every time the sequence of the bands and to assess the reliability of the IOPs. This work focuses the attention on the assessment of the IOPs definition for each sensor, considering the impact of environmental conditions (e.g., different time, exposure, brightness) and different configurations of the FPI camera, in order to rebuild an undistorted hypercube for image processing and object estimation. The aim of this work is to understand if the IOPs are stable over the time and if and which bands can be used as reference for the calculation of the inner parameters for each sensor, considering different environmental configurations and surveys, from terrestrial to aerial applications. Preliminary performed tests showed that the focal length percentage variation among the bands of different experiments is around 1%.

1. INTRUDUCTION

Several applications, such as precision agriculture, environmental monitoring and mapping require Unmanned Aerial Vehicles (UAVs) as one the main tools for high resolution images acquisition (Thenkabail et al., 2014).
The main purposes, in these fields, are to provide reports related to management treatments and environment protection and to supervise the efficient use of resources (Honkavaara et al., 2013).
In order to achieve these aims, for these specific applications, visible bands of traditional sensors cannot properly assess the productivity and stress indicators as multi or hyper spectral sensors (Adão et al., 2017). Indeed, thanks to the hyperspectral sensors, it is possible to obtain the spectral signature with a high spectral resolution (Manolakis 2003). The spectral signature is an important feature to characterize different objects and materials and to identify analysis ranges and to study possible anomalies. The same level of detail is impossible to achieve by multispectral sensors.
Recently, different lightweight, frame-based hyperspectral cameras suitable for UAV surveys were developed. The main difference among common hyperspectral sensors available on the market is related to the acquisition mode. There are four categories of hyperspectral cameras: whisk broom (or point scanning), push broom (or line scanning), single shot or frame-based (Adão et al., 2017). The whisk broom sensors collect all the bands pixel by pixel, storing the data in a band-interleaved-by-pixel (BIP) cube; pushbroom sensors acquire, instead, an entire line-sequence of pixels, which ends up by constituting a band-interleaved-by-line (BIL) cube. The more recent sensors collect spatial and spectral data in a single shot within a single integration period, saving a band sequential (BSQ) cube. The frame-based cameras overcome the slow acquisition problem of the whiskbroom sensors and the saturation or underexposure issues of the push broom. Moreover, the snap shot sensors do not need high precision inertial platform.The problem of external orientation parameters could be solved a posteriori using GCPs (Ground Control Points). Indeed, it is possible to estimate the position of the camera during the acquisition with the coordinates of few GCPs acquired by a Global Satellite Navigation System (GNSS) receiver with a Post Processing Kinematic (PPK) or a Real Time Kinematic (RTK) approach.
Among the frame-based hyperspectral cameras, the Rikola developed by the VTT Technical Research Centre of Finland (Saari et al., 2009) and produced by Senop, is one of the most lightweight sensor with a high spectral resolution (Senop, 2018). This camera is based on tunable filters able to inspect spectral range between 500-900 nm, including two sensors: one sensor (defined as Sensor 1) acquires near infrared bands, from 659.2 nm to 802.6 nm, while the second (Sensor 2) captures visible bands, from 502.8 nm to 635.1 nm. Among the different components of this camera, one of the most important is the Fabry-Perot Interferometer (FPI): this interferometer is composed by two partially reflective parallel plates with variable distance (air gap), controlled by piezoelectric actuators (Saari et al., 2009; Tommaselli et al., 2018). When the electromagnetic radiation affects the plates, many refractions and reflections occur: the constructive interferences that happen within the plates allow certain wavelengths to be transmitted

* Corresponding author

while others are reflected, because the wavelengths are function of FPI gap (air-gap). The incident radiation on this type of camera passes initially through the optical assembly and then through the FPI interferometer, being redirected to two CMOS sensors by means of a beam splitter prism.
The camera is also equipped with a GNSS receiver for georeferencing purposes and an irradiance sensor for external areas subject to the solar lighting. The irradiance sensor, more in detail, measures down welling irradiance and it is useful for in-situ radiometric calibration (Hakala et al., 2013).
Rikola can acquire sequences of two dimensional image bands (with defined different ranges), that are time-dependent. Thus, if data are collected using a moving platform, the hyperspectral cube generation requires a band-coregistration process. While the frame geometry makes feasible the simultaneous determination of exterior orientation parameters (EOPs) of all images by bundle block adjustment, several issues must be addressed for the proper definition and estimation of the inner orientation parameters (IOPs), due to internal geometry.
Therefore, the development of an appropriate geometric calibration approach and a validation procedure are needed. Olivera et al. (2018) addressed the problem of camera calibration for FPI sensors (Senop, 2018) and analyzed the variation of IOPs in each band. The work underlined that the major difference in the IOPs occurs because the FPI changes slightly the optical path. Moreover, the authors highlighted that the changes are more prominent among the two sensors, basically because they are not perfectly aligned.
Due to the possibility to adjust the sets of the bands depending on the case study, it is unfeasible to generate IOPs for all possible sets of configurations.
The work is focused on the assessment of the IOPs estimation for each sensor, by analyzing the impact of different environmental conditions (e.g., different time, exposure, brightness), in order to rebuild an undistorted hypercube and to understand if it is possible to apply the same sets of parameters for different survey configurations. Thus, the aim of this work is to verify if the IOPs are stable over the time and if one or more bands can be used as reference for the estimation of the internal parameters for each sensor, considering different environmental configurations.

2. METHODOLOGY

Before using this camera for surveying applications, it is important to have an appropriate calibration of lenses and sensors that allows to obtain more accurate results in terms of geometry estimation. Indeed, the geometric calibration allows to estimate the distortions and deformation parameters.
In order to verify the reliability of the inner orientation parameters and to evaluate them in different environmental conditions, a methodology has been proposed, based on these main steps:

1) hypercube acquisition;
2) split of hypercubes in single band images;
3) calibration procedure for each band;
4) generation of undistorted images;
5) reconstruction of a new undistorted hypercube.

In details:

1) The hypercube acquisition was designed according to the geometrical definition of the problem considered and to the resolution of the images. Transversal and longitudinal overlaps between the sequential images were guaranteed. The close-range photogrammetry with convergent images was performed using the rules for the Structure for motion acquisitions (Kraus, 1997) .
2) The cubes were collected in .bsq format by the camera. However, before any other operation, they were converted into GeoTIFF images using the ENVI software (version 4.7 2009) and then processed by the Matlab "Camera Calibrator" toolbox. Each acquired hypercube was divided in single band images with a dedicated algorithm in Matlab®, to estimate the inner orientation parameters for each band.
3) In order to apply a self–calibration (Clarke, 1998) approach, a calibration panel was used, in which the coordinates of the target are known with an accuracy of about 0.03 mm (Remondino, 2006). Among the several tools available for the camera calibration, the Matlab calibration tool has been chosen with the algorithm proposed by Bouguet (2015). The module includes the pinhole camera model with the estimation of the affine sensor distortions and lens distortions (Zhang , 2000; Heikkila and Silven, 1997). The solution requires the estimation of the inner orientation parameters in order to reconstruct the inner geometry of the camera using the position of the principal point (ξ_0, η_0) in the image coordinate system, the focal length (c), the polynomial coefficients, k_1, k_2, k_3 of the radial distortions, the tangential distortions P_1, P_2 and the skew (Brown, 1971).
   The radial distortion curves could be represented as a function of the radial distance (ρ) (1) (Kraus, 1997; Ghinamo et al., 2014):

$$\delta_r = k_1 \rho^3 + k_2 \rho^5 + k_3 \rho^7 + \dots \quad (1)$$

$$\rho = \sqrt{(x^2 + y^2)} \quad (2)$$

   In the Matlab "Camera Calibrator" tool, the (x,y) image coordinates are normalized considering the ratio between the pixel coordinates and the focal length expressed in pixels (Bouguet, 2015).
4) Undistorted images can be generated using the parameters estimated with the calibration procedure. This step is still accomplished using the Matlab "Camera Calibrator".
5) The undistorted images are merged in a single hypercube with a Matlab algorithm developed by the authors.

The whole procedure has been validated considering different 3D models generated by Agisoft Photoscan software version 1.3.4 (Agisoft Photoscan), applying the estimated camera parameters.

3. HYPERSPECTRAL CALIBRATION

The current investigation involved the acquisition and the analyses of different sets of hypercubes. Indeed, to evaluate the camera parameters in different environmental conditions, the methodology was also applied in 3 different time intervals:

1) Test 1 (T1) was performed in indoor environment considering uncontrolled illumination and exposure;
2) Test 2 (T2) was conducted in indoor conditions with a controlled illumination and exposure. To reproduce

the perfect illumination and exposure conditions, fluorescent lamps were used, as shown in Figure 1;

3) Test 3 (T3) was carried out in an outdoor environment, with standard illumination and common exposure conditions, as shown in Figure 2.

The calibration was performed using a calibration panel with an internal array of black and white squares (size of 10 cm).

The three tests were performed at Photogrammetry, Geomatics and GIS Laboratory of DIATI (Department of Environment, Land and Infrastructure Engineering) at Politecnico di Torino (Italy).



Figure 1. The acquisition of a dataset in indoor environment, considering controlled illumination and exposure values (T2)



Figure 2. The acquisition of a dataset in outdoor environment (T3)

For each configuration, according to the close-range photogrammetry procedure described in the Methodology section, all cubes were collected from an average distance of 1.5 m changing the positions and the rotations of the camera. The Figure 3 represents one of the considered schema of camera positions.

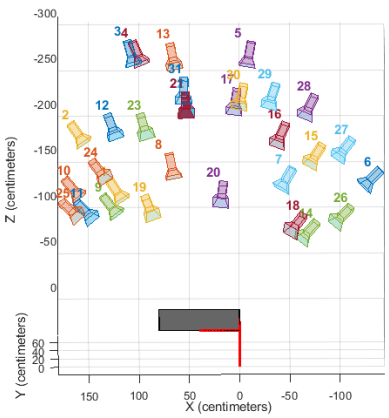


Figure 3 Example of a set of acquired images during a preformed test

The camera was used in manual mode connected to the computer through an USB cable. The selected image resolution was 1010x1010 pixels. The integration time was set based on the illumination condition of the environment. The sequence of the bands was automatically generated using the Rikola Hyperspectral Imager software v2.0. The spectral range was considered starting from a wavelength of 502 nm, up to 806 nm, with a wavelength step of 12 nm and a Full With Half Maximum resolution (FWHM, where Wide means low gap index). These parameters were chosen to cover the whole range of the spectral range. Moreover, for each test, the integration time was set according to the illumination and the environmental conditions.

The obtained cubes were composed by 24 bands in which of 13 bands were collected by the Sensor 2 and 11 bands by Sensor 1. The main features of each test are summarized in **Errore. L'origine riferimento non è stata trovata.**.

N. of tests	N. of cubes	Dimension (GB)	Environmental conditions	Integration time
T1	21	1.91	Indoor uncontrolled	500 ms
T2	31	2.82	Indoor- controlled	1000 ms
T3	29	2.64	Outdoor	10 ms

Table 1 Calibration tests.

In order to have the same number of cubes, 21 cubes for each test were chosen. As mentioned in the Methodology section, each cube was split into 24 different images for performing the calibration procedure. The calibration tool converted the images from 12-bit images in 8-bit images and for each test 504 images (3.83 GB) were processed. The procedure allowed to estimate the coordinates of the principal point and the focal length, the radial distortion coefficients, and the tangential distortions.

4. RESULTS

This section presents the results of the calibration procedure for all tests performed.

Figure 4 shows the focal length values for each configuration. All values in this figure represent the average between the c_x and c_y values estimated by the Matlab "Camera Calibrator" tool.

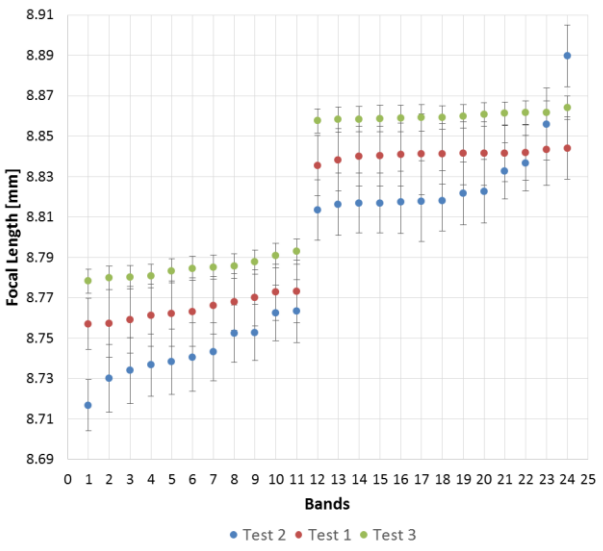


Figure 4. The distribution of the focal length estimations in function of bands

As it is possible to see from Figure 4, the distribution of the focal length estimation can be summarized in two main clusters: one for the sensor 2 (left side) the other one for sensor 1 (right side).
This behavior is valid for all datasets: the values obtained from T2 are closed to the T3 results, instead T1 values are different. Another interesting aspect that can be seen from Figure 4 is that T1 minimum and maximum values, are quite different to the values obtained from T2 and T3. The focal length values obtained in T3 are the most equivalent to the nominal focal length is 9 mm (Table 2).
Figure 5, Figure 6 and Figure 7 illustrate the principal point coordinates (ξ_0, η_0) for each configuration and for each sensor.

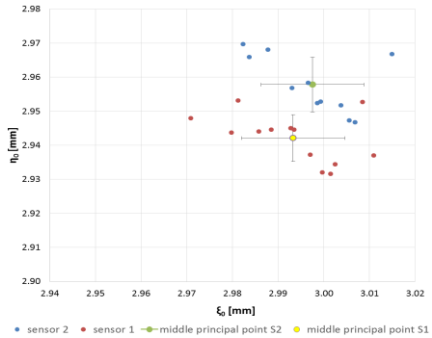


Figure 5 Distribution of the Principal Point coordinates considering T1.

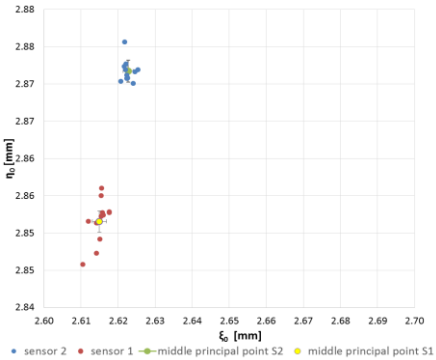


Figure 6. Distribution of the Principal Point coordinates considering T2.

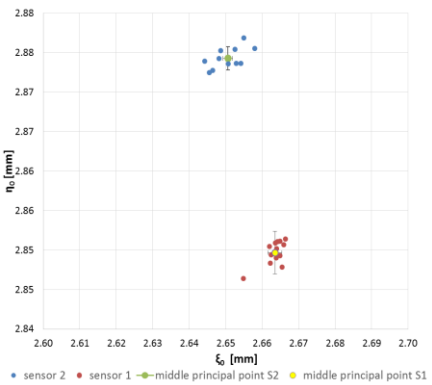


Figure 7. Distribution of the Principal Point coordinates considering T3

The division in two different clusters based on the sensors is clear: all blue points were collected by sensor 2 while all red ones by sensor 1. Indeed, the principal point locations are spread around the mean values for each sensor.

It is important to underline that while the values of T2 and T3 are in the same range of value in ξ_0 and η_0, the T1 values are in another range. Probably, the differences between the focal length and the standard deviations obtained in T2 and T3 are no notable than those in T1. The main reason of this difference is related to the environmental conditions in which the tests were performed.
Table 2 shows the average values of the estimated principal point for the two Sensors (1, 2) with the related Root Mean Square (RMS) and the average values of the focal length in the different tests.

Test/ Sensor	ξ_0 [mm]	$RMS_{\xi 0}$ [mm]	η_0 [mm]	$RMS_{\eta 0}$ [mm]	c [mm]	RMS_c
T1-S1	2.998	±0,010	2.942	±0,006	8.786	± 0,003
T1-S2	2.993	±0,011	2.958	±0,008		
T2- S1	2.615	±0,002	2.852	±0,003	8.803	±0,001
T2- S2	2.623	±0,001	2.872	±0,001		
T3- S1	2.664	±0,003	2.850	±0,001	8.822	±0,001
T3- S2	2.651	±0,004	2.874	±0,001		

Table 2. Main statistical parameters related to Principal Point coordinates and focal length

The differences of the average principal point coordinates between all configurations are less than 0.003 mm for ξ_0 and 0.02 mm for η_0.
In order to evaluate the focal length variation at different distances, the cubes of the test 3 were used. Indeed, during the test 3, two different cubes were collected from a distance of 1.5 m and 3 m.
The estimated value of the focal length of these cubes was compared with the focal length of three cubes acquired at 1.5 m. The results of this analysis are collected in the Table 3. Even if the distance increase, no particular differences can be obtained both in terms of precision and accuracy.

Test	Distance [m]	Focal Length [mm]
3a	3	8.87 ± 0.028
3b	1.5	8.83 ± 0.006

Table 3 Focal length values at different distances

To give a complete description of the camera parameters, radial and tangential distortions were also analyzed. As shown in Figure 8,
Figure 9 and Figure 10, the radial distortions have a “barrel” shape.

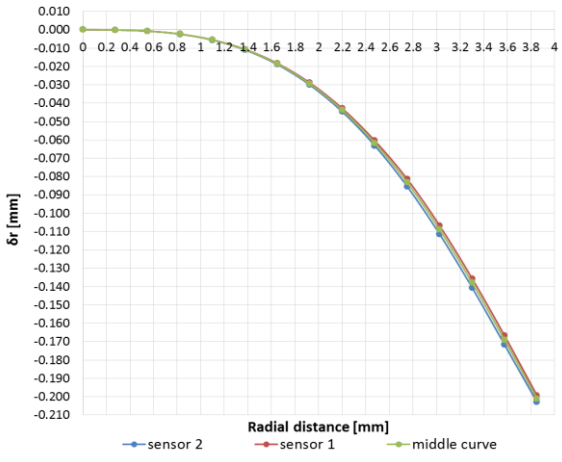


Figure 8 Radial Distortion Curves- T1

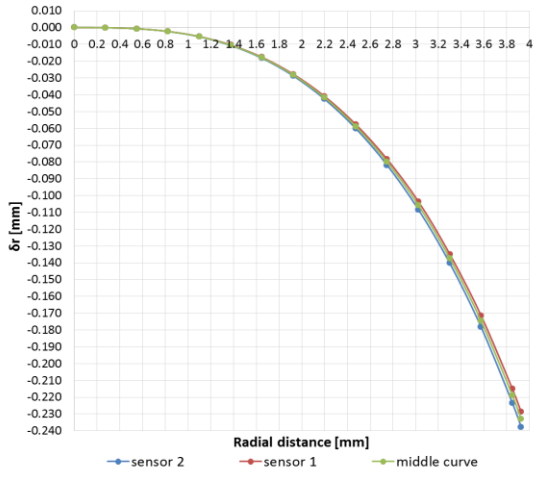


Figure 9 Radial Distortion Curves- T2

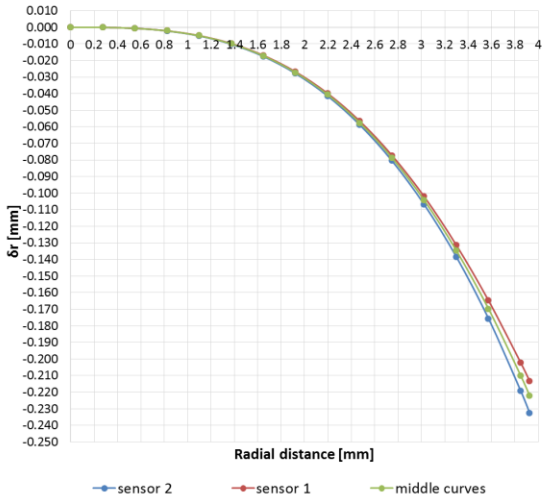


Figure 10 Radial Distortion Curves- T3

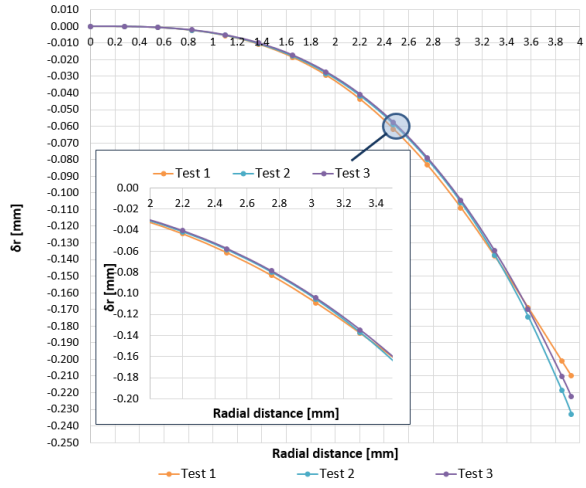


Figure 11 Middle Radial Distortion Curves- T1, T2, T3

The results of the T2 and T3 tests are very similar. The differences between the maximum radial coefficients obtained from these two datasets are less than 0.001 mm. However, the maximum radial coefficient obtained from T1 is around 0.20 mm, that is quite different if compared to those obtained in the other two cases (0.23 mm). Figure 11 shows a similar behavior of the T2 and T3 middle radial curves, instead the T1 middle curve is quite different. Generally, the tangential distortion coefficients are smaller than the radial distortion ones, thus they could be considered negligible.

Test/ Sensor	k_1 [pixel $^{-2}$]	k_2 [pixel $^{-4}$]	k_3 [pixel $^{-6}$]	P_1 [pixel $^{-1}$]	P_2 [pixel $^{-1}$]
T1-S1	-0.31594	-0.00457	1.37737	-0.00011	-0.00014
T1-S2	-0.32468	-0.11646	2.12995	-0.00094	-0.00136
T2-S1	-0.31645	0.35366	-1.15345	-0.00104	-0.00149
T2-S2	-0.32499	0.31637	-1.02630	-0.00094	-0.00136
T3-S1	-0.29504	0.00114	0.53616	-0.00011	-0.00074
T3-S2	-0.30943	0.11010	-0.27701	-0.00003	-0.00064

Table 4. Tangential distortions coefficients in function of tests and sensors considered

Table 4 shows that the results of T1 and T3 are similar for both P1 and P2 coefficients. However, the differences among T1, T2 and T3 are very small.
Analyzing the IOPs estimation, one set of IOPs was chosen for each band to generate the undistorted images. The results of T3 were selected in this step because the environmental conditions are more comparable to the standard conditions in which the camera will be used.

5. VALIDATION

The validation procedure was performed using the Agisoft Photoscan version 1.3.4. This software was chosen because it is one the most common software used for the photogrammetric 3D model creation. Both distorted and undistorted images of band 1 were processed to generate a 3D model, for estimating a distance between points A and B, and A and C, respectively as shown in Figure 12.

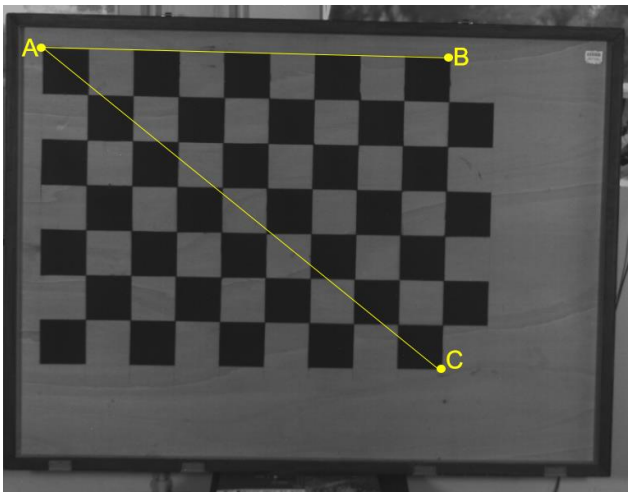


Figure 12 Reference distance

Three different models were generated: D1, where the camera parameters were estimate by the software, D2 and UnD3 where the camera parameters were considered as fixed. The only difference between D2 and UnD3 is that in the first case the images are distorted while in UnD3 all images are undistorted. For all cases, the selected IOPs are the ones calculated by Matlab. Certainly, the parameters are related to the selected band.
The selected parameters are summarized in the following Table 5.

Pixel [mm]	0.0055
Focal length [pixel]	1592.22
ξ_0 [pixel]	476.49756
η_0 [pixel]	521.8850
k_1 [pixel $^{-2}$]	-0.3027
k_2 [pixel $^{-4}$]	-0.0191
k_3 [pixel $^{-6}$]	- 1.5835
P_1 [pixel $^{-1}$]	0.0002
P_2 [pixel $^{-1}$]	0.0005

Table 5 Calibration parameters fixed during the Photoscan process

The results of the validation procedure are summarized in the Table 6.

Parameters (cm)	D1	D2	UnD3
x_A	0	0	0
y_A	0	0	0
x_B	89.995	90.001	90.003
y_B	0.002	0.001	0.001
x_C	99.999	100.050	103.000
y_C	69.920	69.990	65.530
$Dist_{AB}$	89.995	90.001	90.003
Real $Dist_{AB}$	90	90	90
Difference $Dist_{AB}$	0.004	0. 001	0. 003
$Dist_{AC}$	122.019	122.100	122.079
Real $Dist_{AC}$	122.066	122.066	122.066
Difference $Dist_{AC}$	0.005	0.003	-0.013

Table 6 Distance measurements

The difference between the real (reference, measured by tape) and the calculated distances are small. However, the same tests should be performed in a real case at the real distance of camera acquisition from a UAV system.

6. CONCLUSIONS

This study aims to test a methodology to evaluate the IOPs estimation of the Rikola sensors, their reliability along the time considering also different environmental conditions. Three tests were performed in different times: two considering an indoor environment (uncontrolled and controlled environmental conditions) and one in outdoor environment (real case).
After the data acquisition, the IOPs estimation of each hypercube for single band was computed and analyzed.
The results of the validation procedure underlined that an appropriate calibration procedure can improve the quality of the geometric measurements on the photogrammetric model generated by the hyperspectral images.
The whole process demonstrates that the calibration in standard conditions is quite stable over the time for each sensor. Instead, at same time, it is possible to perform an on-field calibration, even if the environmental conditions are different from the standard ones, e.g., differences in terms of temperatures or illumination conditions. Possible future developments of this work could be the investigation of the influence of thermal conditions in the camera parameters estimation and the possibility to perform the in-situ radiometric calibration of the camera.

ACKNOWLEDGEMENTS

This project was carried out thanks to funding from MANUNET research program of international interest called “Spectral Evidence of Ice (SEI)” and the PoliTO Interdepartmental Centre for Service Robotics (PIC4SeR).

REFERENCES

Adão, T., Hruška, J., Pádua, L., Bessa, J., Peres, E., Morais, R., & Sousa, J. J. (2017). Hyperspectral imaging: A review on UAV-based sensors, data processing and applications for agriculture and forestry. *Remote Sensing*, *9*(11), 1110. doi.org/10.3390/rs9111110.

Agisoft Photoscan, https://www.agisoft.com/ (31/03/2019).

Brown, D. C.. (1971). Close-range camera calibration. *Photogramm. Eng*, *37*(8), 855-866.

Bouguet, J. Y., (2015), Camera Calibration Toolbox for Matlab. Computational Vision at the California Institute of Technology. Camera Calibration Toolbox for MATLAB.

Clarke, T. A., & Fryer, J. G. (1998). The development of camera calibration methods and models. *The Photogrammetric Record*, *16*(91), 51-66.

de Oliveira, R. A., Tommaselli, A. M., & Honkavaara, E. (2016). Geometric calibration of a hyperspectral frame camera. *The Photogrammetric Record*, *31*(155), 325-347.

Ghinamo, Giorgio, et al. (2014). The MPEG7 visual search solution for image recognition based positioning using 3D models. In: *Proceedings of the 27th International Technical Meeting of The Satellite Division of the Institute of Navigation, Tampa, FL, USA*. 2014. p. 8-12.

Hakala, T., Honkavaara, E., Saari, H., Mäkynen, J., Kaivosoja, J., Pesonen, L., & Pölönen, I. (2013). Spectral imaging from UAVs under varying illumination conditions. In *International Archives of the Photogrammetry, Remote Sensing and Spatial Information Sciences*. International Society for Photogrammetry and Remote Sensing (ISPRS).

Honkavaara, E., Saari, H., Kaivosoja, J., Pölönen, I., Hakala, T., Litkey, P., ... & Pesonen, L. (2013). Processing and assessment of spectrometric, stereoscopic imagery collected using a lightweight UAV spectral camera for precision agriculture. *Remote Sensing*, *5*(10), 5006-5039.

Heikkila, J., and O. Silven. (1997), A Four-step Camera Calibration Procedure with Implicit Image Correction. *IEEE International Conference on Computer Vision and Pattern Recognition*..

Kraus K., 1997, Photogrammetry II, Advanced method and application, Ummler/Bonn, ISEN 3-427-786943.

Manolakis, D., Marden, D., & Shaw, G. A. (2003). Hyperspectral image processing for automatic target detection applications. *Lincoln laboratory journal*, *14*(1), 79-116.

Remondino, F., & Fraser, C. (2006). Digital camera calibration methods: considerations and comparisons. *International Archives of Photogrammetry, Remote Sensing and Spatial Information Sciences*, *36*(5), 266-272.

Saari, H., Aallos, V. V., Akujärvi, A., Antila, T., Holmlund, C., Kantojärvi, U., Ollila, J., (2009). Novel miniaturized hyperspectral sensor for UAV and space applications. In SPIE

Europe Remote Sensing. International Society for Optics and Photonics, 74741M-74741M-12.

Senop, n.d. Rikola Hyperspectral camera (2018), Optron. Hyperspectral. URL: http://senop.fi/optronicshyperspectral# hyperspectralCamera

Thenkabail, P.S.; Gumma, M.K.; Teluguntla, P.; Mohammed, I.A. (2014), *Hyperspectral Remote Sensing of Vegetation and Agricultural Crops. Photogramm. Eng. Remote Sens. 2014*, 80, 697–723.

Tommaselli, A. M., Oliveira, R. A., Nagai, L. Y., Imai, N. N., Miyoshi, G. T., Honkavaara, E., & Hakala, T. (2015). Assessment of bands coregistration of a light-weight spectral frame camera for UAV. In *GeoUAV-ISPRS Geospatial Week*.

Tommaselli, A. M. G., Berveglieri, A., Oliveira, R. A., Nagai, L. Y., & Honkavaara, E. (2016). Orientation and calibration requirements for hyperspectral imaging using UAVs: a case study. *International Archives of the Photogrammetry, Remote Sensing & Spatial Information Sciences*, *40*.

Tommaselli, A. M. G., Santos, L. D., de Oliveira, R. A., & Honkavaara, E. (2018, July). Refining the geometric calibration of a hiperspectral frame camera with preliminary bands coregistration. In *IGARSS 2018-2018 IEEE International Geoscience and Remote Sensing Symposium* (pp. 6468-6471). IEEE.

Zhang, Z. "A Flexible New Technique for Camera Calibration." IEEE Transactions on Pattern Analysis and Machine Intelligence. Vol. 22, No. 11, 2000, pp. 1330–1334.